Microlensing as a probe of the Galactic structure
20 years of microlensing optical depth studies

Marc Moniez

Abstract Microlensing is now a very popular observational astronomical technique. The investigations accessible through this effect range from the dark matter problem to the search for extra-solar planets. In this review, the techniques to search for microlensing effects and to determine optical depths through the monitoring of large samples of stars will be described. The consequences of the published results on the knowledge of the Milky-Way structure and its dark matter component will be discussed. The difficulties and limitations of the ongoing programs and the perspectives of the microlensing optical depth technique as a probe of the Galaxy structure will also be detailed.

Keywords microlensing · dark matter · Galactic structure

1 Introduction

In 1936 A. Einstein published a half-page note in Science entitled *"lens-like action of a star by the deviation of light in the gravitational field"* [48], with this final comment: *"There is not great chance of observing this phenomenon."* According to J. Renn [92] the effect was already predicted by A. Einstein as early as 1912, before completion of the general theory of relativity. S. Liebes [71] considered again the properties of the gravitational lenses in 1964, and studied the possibility to detect high magnification events. Furthermore, this author already mentioned the possibility to detect invisible compact objects through microlensing. In 1986, B. Paczyński [81] pointed out the possibility of using the gravitational microlensing effect to detect massive compact objects of the Galactic halo in the direction of the Magellanic Clouds.

M. Moniez
Laboratoire de l'Accélérateur Linéaire, IN2P3 CNRS, Université Paris-Sud, 91405 Orsay Cedex, France
Tel.: +33-1-64468344
Fax: +33-1-64468397
E-mail: moniez@lal.in2p3.fr

In 1989, the raising question amongst astrophysicists was the nature of dark matter within the Milky-Way halo. WIMPS[1] search experiments were already looking for exotic dark matter, but it was realized at this epoch that the question of today's nature of the majority of the baryons (at $z = 0$) —still pending— could be addressed through the microlensing technique. From 1989, several groups started survey programs to search for compact halo objects within the Galactic halo. The challenge for the EROS and MACHO teams was to clarify the status of the missing hadrons in our own Galaxy. In september 1993, three teams, EROS [24], MACHO [9] and OGLE [111] discovered the first microlensing events in the directions of the Large Magellanic Cloud and the Galactic Center. Since these first discoveries, thousands of microlensing effects have been detected in the direction of the Galactic Center (GC) together with a handful of events towards the Galactic Spiral Arms (GSA) and the Magellanic Clouds.

Probing Galactic structure with microlensing: Microlensing has proven to be a powerful probe of the Milky-Way structure, and not only for the hidden baryonic matter. Searches for microlensing towards the Magellanic Clouds (LMC, SMC) and M31 provide optical depths through the Galactic halo, allowing one to study dark matter under the form of massive compact objects. Searches towards the Galactic plane (Galactic Center, GC and Galactic Spiral Arms, GSA) allow one to measure the optical depth due to ordinary stars in the Galactic disk and bulge. Kinematical models as well as mass functions can also be tested through the event duration distributions. In a few special cases called "exotic" events, more specific information on the lensing system has been obtained; unfortunately they don't yet provide sufficiently large samples to extract reliable information on the Galactic structures.

This article reviews the optical depth measurements, which are the instantaneous probabilities for a point-source of a target to be magnified by a factor larger than 1.34. The description of the observational devices and of the analysis techniques will be given, followed by a discussion about the main difficulties and limitations which can be overcome in future surveys. The consequences of the optical depth measurements on the Galactic structure knowledge will also be reviewed, with the first connections that can be established between the kinematics of the Galactic structures and the duration distributions. We will conclude with a prospective on the future surveys and a description of the potential of microlensing searches in infrared and of "fine" searches, sensitive to exotic events, providing valuable extra information.

2 Microlensing basics

Gravitational microlensing effect occurs when a massive compact object passes close to the line of sight of a star and produces gravitational images that are not intercepted by the massive object (no eclipse), but that cannot be

---

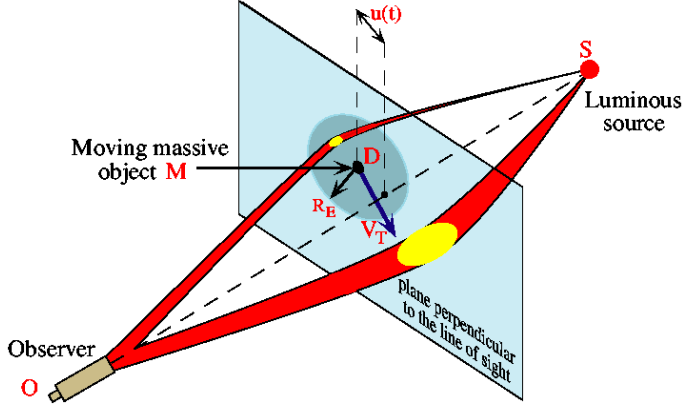[1] Weakly Interacting Massive ParticleS

Fig. 1 *Principle of the microlensing effect: As the deflector D of mass M moves with a transverse relative speed V_T, the impact parameter $u(t)$ changes with time, and so does the magnification of the source.*

separated in telescopes (no multiple images)(see Fig. 1). The detection of such a coincidence is then possible only if a measurable magnification variation occurs during the observation time. The details on the formalism associated with this phenomenon can be found in [100] and we will only provide here a few basic tools. In the approximation of a single point-like object acting as a deflector on a single point-like source, the total magnification of the source luminosity at a given time t is the sum of the contributions of two images, given by

$$A(t) = \frac{u(t)^2 + 2}{u(t)\sqrt{u(t)^2 + 4}} \ , \tag{1}$$

where $u(t)$ is the distance of the deflecting object to the undeflected line of sight, expressed in units of the "Einstein Radius" $R_{\rm E}$:

$$R_{\rm E} = \sqrt{\frac{4GM}{c^2}D_S x(1-x)} \simeq 4.54 \ A.U. \times \left[\frac{M}{M_\odot}\right]^{\frac{1}{2}} \left[\frac{D_S}{10 \ kpc}\right]^{\frac{1}{2}} \frac{[x(1-x)]^{\frac{1}{2}}}{0.5}. \tag{2}$$

Here G is the Newtonian gravitational constant, D_S is the distance of the observer to the source and $x D_S = D_L$ is its distance to the deflector of mass M. The motion of the deflector relative to the line of sight makes the magnification vary with time. Assuming a deflector moving at a constant relative transverse speed v_T, reaching its minimum distance u_0 (impact parameter) to the undeflected line of sight at time t_0, $u(t)$ is given by

$$u(t) = \sqrt{u_0^2 + ((t - t_0)/t_{\rm E})^2}, \tag{3}$$

where $t_{\rm E} = R_{\rm E}/v_T$, the "lensing time scale", is the only measurable parameter bringing useful information on the lens configuration in the approximation of

simple microlensing:

$$t_{\mathrm{E}} \sim 79. \; days \left[\frac{v_T}{100 \, km/s}\right]^{-1} \left[\frac{M}{M_\odot}\right]^{\frac{1}{2}} \left[\frac{D_S}{10 \, kpc}\right]^{\frac{1}{2}} \frac{[x(1-x)]^{\frac{1}{2}}}{0.5} \; . \qquad (4)$$

2.1 Microlensing event characteristics

The so-called simple microlensing effect (point-like source and point-like lens with uniform relative motion with respect to the line of sight) has some characteristic features which allow one to discriminate it from any known intrinsic stellar variability :

 − The event is singular in the history of the source (as well as of the deflector).
 − The gravitational origin of the effect implies that the magnification is independent of the color.
 − The magnification is a known function of time, depending on only 3 parameters $(u_{min}, t_0, t_{\mathrm{E}})$, with a symmetrical shape.
 − As the geometric configuration of the source-deflector system is random, the impact parameters of the events must be uniformly distributed.
 − The passive role of the lensed stars implies that their population should be representative of the monitored sample, particularly with respect to the observed color and magnitude distributions.

This simple microlensing description can be broken in many different ways: the lens may be a double system [75], or the source may be an extended object [120], or the relative motion with respect to the line of sight may deviate from a uniform motion due either to the rotation of the Earth around the Sun (parallax effect) [55] [66], or to an orbital motion of the source or of the lens around the center-of-mass of a multiple system [79]. All these deviations have been observed and will be discussed further in this issue (see the contribution of M. Dominik [45]). The interest of these "exotics" comes from the extra-information on the lensing configuration that can be obtained in such specific cases.

2.2 The observables: optical depth, event rate and t_{E} distribution

The optical depth up to a given source distance D_S is defined as the instantaneous probability for the line of sight of a target source to intercept a deflector's Einstein disk, that corresponds to a magnification $A > 1.34$. Assuming that the distribution of the deflector masses is described by a density function $\rho(D_L)$ and a normalized mass function $\mathrm{d}n_L(D_L, M)/\mathrm{d}M$, this probability is:

$$\tau(D_S) = \int_0^{D_S} \int_{M=0}^{\infty} \pi \theta_E^2 \times \frac{\rho(D_L) D_L^2}{M} \frac{\mathrm{d}n_L(D_L, M)}{\mathrm{d}M} \mathrm{d}M \mathrm{d}D_L \, , \qquad (5)$$

where $\theta_E = R_{\mathrm{E}}/D_L$ is the angular Einstein radius of a lens of mass M located at D_L. The second term of the integral is the differential number of these

lenses per mass unit and per solid angle. As the solid angle of the Einstein disk is proportional to the deflectors' mass M, this probability is found to be independent of the deflectors' mass function:

$$\tau(D_S) = \frac{4\pi G D_S^2}{c^2} \int_0^1 x(1-x)\rho(x)\mathrm{d}x \,, \qquad (6)$$

where $\rho(x)$ is the mass density of deflectors located at a distance xD_S. The mean optical depth towards a given population defined by a distance distribution $\mathrm{d}n_S(D_S)/\mathrm{d}D_S$ of target stars is defined as

$$< \tau >= \frac{\int_0^\infty \frac{\mathrm{d}n_S(D_S)}{\mathrm{d}D_S}\tau(D_S)D_S^2\,\mathrm{d}D_S}{\int_0^\infty \frac{\mathrm{d}n_S(D_S)}{\mathrm{d}D_S}D_S^2\,\mathrm{d}D_S}. \qquad (7)$$

The *measured* optical depth associated to microlensing events observed in a population of N_{obs} stars monitored for a duration ΔT_{obs} is given by [2]

$$\tau = \frac{1}{N_{obs}\Delta T_{obs}}\frac{\pi}{2}\sum_{events}\frac{t_{\mathrm{E}}}{\epsilon(t_{\mathrm{E}})}, \qquad (8)$$

where $\epsilon(t_{\mathrm{E}})$ is the average detection efficiency of microlensing events with a time scale t_{E} (see the precise definition in Sect. 4.4).

The calculated optical depth does not depend on the deflectors' mass function, but the measured optical depth, that takes into account the mean detection efficiency $\epsilon(t_{\mathrm{E}})$, can be biased by this mass function, in particular because the detection function vanishes for very short or very long duration events. This fact makes impossible a perfect compensation of the inefficiencies. If many deflectors are light (resp. heavy) enough to produce extremely short (resp. long) duration events that cannot be detected, the measured optical depth will clearly be underestimated. This is why collaborations often indicate that their results are valid within a given duration domain. The control of the detection efficiency —that is needed to get reliable optical depths and rate estimates— is one of the most delicate aspects of the survey searches.

Event rate: Contrary to the optical depth, the microlensing event rate depends on the deflectors' mass distribution as well as on the velocity and spatial distributions. The global *measured* event rate, corrected for the detection efficiency, is

$$\Gamma = \frac{1}{N_{obs}\Delta T_{obs}} \times \sum_{events}\frac{1}{\epsilon(t_{\mathrm{E}})}. \qquad (9)$$

This event rate and the duration distributions are used to constrain the mass function and the kinematics of the lensing structures [59] [121]. Such studies will only be briefly mentioned in this review, as the available efficiency controlled statistics are still very limited for quantitative comparisons.

---

[2] The product $N_{obs} \times \Delta T_{obs}$ is called the exposure.

3 Observations

Three types of programs can be distinguished. The two first ones, that can be called "survey programs", monitor large samples of stars that are either identified in the images (catalog survey programs) or that are not identified (pixel survey programs). The third type can be considered as "follow-up programs" that finely monitor individual events detected by the early warning systems of the survey programs. In this review, we will only discuss the catalog survey programs with brief mentions of the other types that are discussed in details in the other contributions of this volume; in particular, results from the M31 pixel surveys are discussed in the Calchi Novati's review [35], and the follow-up programs are reviewed by M. Dominik [45].

Table 1 lists the characteristics of the devices used in the catalog survey programs. The common requirements of these surveys are the monitoring of a very large number of stars, with the best time-sampling and the best photometric resolution that can be achieved. These requirements drive the main specifications of the instruments: they all monitor wide crowded fields with broad passband filters –to get a large photon flux. The achromaticity of the microlensing events further supports this use of wide passband filters; since the ratio of luminosities does not depend on the wavelength, the signal significance increases with the photon flux. These surveys use in general at least two different passbands to make easier the identification of achromatic events. Figures 3 and 5 show the fields monitored by the different teams towards the Galactic plane and the Large Magellanic Cloud.

EROS: Expérience de Recherche d'Objets Sombres. After a first phase started in 1990, using ESO-Schmidt (1m) telescope photographic plates digitized with the MAMA machine and a 16 CCDs camera [25] [23], the EROS team used the 1m (F/5) MARLY telescope installed at La Silla observatory (Chile) from July 1996 to February 2003, with a dichroic beam-splitter allowing the simultaneous imaging in two wide pass-bands (EROS-blue and EROS-red) of a $0.7°(\alpha) \times 1.4°(\delta)$ field [26]. Photons were collected by two cameras equipped with eight $2K \times 2K$ LORAL CCDs each. Exposure times ranged typically from 2 to 5 minutes and were optimized to maximize the global significance of the photometric measurements taken during microlensing magnifications. EROS monitored LMC and SMC, the Galactic Center (GC), and four directions in the Galactic Spiral Arms (GSA).

MACHO: MAssive Compact Halo Objects. From June 1992 to January 2000 the MACHO team used a 1.27 m (F/3.9) dedicated telescope [67], also equipped with a dichroic beam-splitter and two cameras of four $2K \times 2K$ LORAL CCDs each [102] [76]. This setup, installed at Mount Stromlo (Australia), provided simultaneous blue and red band photometry and covered a field of $0.7°(\alpha) \times 0.7°(\delta)$ with a pixel size of 0.62 arcsec. The LMC, SMC as well as the Galactic Center have been monitored for microlensing searches. The observing strategy changed during the project and the sampling of the Galactic fields varied from a few observations per year to daily observations.

Table 1 Experimental setups devoted to microlensing surveys, with the telescope diameter, the list of the filters, the total number of pixels, the field covered by the detector, the list of surveyed targets with the corresponding monitored fields, numbers of monitored stars, approximative average sampling and observation epochs. The indicative sampling values are averaged over the observation seasons or during the observation nights.
Note: the MACHO SMC data were lost during the Mount Stromlo fire of 18 January 2003.

Set-up	telesc. filters	pixels $\times 10^6$	detector field (°)	target	field deg^2	stars $\times 10^6$	approx. sampling	obs. dates
EROS1 plates	1 m R/B	1000	5.2×5.2	LMC	27.	4.2	3 days	90-93
EROS1 CCD	0.4 m R/B	4	0.4×1.1	LMC	0.44	0.1	20 min.	91-94
				SMC	0.44	0.1	20 min.	93-95
EROS2	1 m I/V	2×32	0.7×1.4	LMC	84.	29.2	3 days	96-02
				SMC	9.	4.2	3 days	96-02
				GC	66.	60.	3 days	96-02
				GSA	20.1	12.9	3 days	96-02
MACHO	1.27 m R/B	2×16	0.7×0.7	LMC	14.7	11.9	4 days	92-99
				SMC	3.	2.2	3 days	93-96
				GC	48.	50.2	3 days	92-99
OGLE I	1 m I	4	0.25×0.25	GC	1.25	1.5	3 days	92-95
OGLE II	1.3 m I/B/V	4	0.24×0.95 drift-scan	GC	11.	20.5	3 days	97-00
				LMC	4.7	5.5	3 days	96-00
				SMC	2.4	2.2		
OGLE III	1.3 m I/V	64	0.58×0.58	LMC	38.	total 120.	2 days	01-09
				SMC	13.			
				GC	35.			
DUO plates	1 m R/B	1000	5.2×5.2	GC	27.	13.	1 day	94
MOA1-cam1	0.61 m B/R	9	(1.×1.)/4	LMC	3.5	1.	3 hours	95-98
				SMC	2.8	0.4	3 hours	95-98
MOA1-cam2	0.61 m B/R	24	0.92×1.38	GC	20.	5.	2 hrs	98-05
				LMC	20.	3.	1 day	98-05
				SMC	10.	1.	1 day	98-05
MOA2-cam3	1.8 m R/V/I	80	1.32×1.65	GC	48.	50.	1 hr	05-
				LMC	31.	50.	1 hr	05-
				SMC	4.4	5.	1 day	05-
Super-MACHO	4 m VR	64	0.57×0.57	LMC	22.	100.	2 days	01-05

OGLE: Optical Gravitational Lensing Experiment. After a first phase started in 1992 [110], making use of a 1m (F/7) telescope in Las Campanas (Chile) to monitor the Galactic Center, the OGLE team has built its own dedicated instrument, using a 1.3m (F/9.2) telescope, equipped with a thinned CCD camera of $2K \times 2K$ pixels and a filter wheel with standard UBVRI filters [108]. The system operated in drift-scan mode with the telescope drifting in declination at a rate of a few arc-seconds per time second. In these conditions a single image covered a field of $0.25°(\alpha) \times 0.9°(\delta)$ with a pixel of 0.4 arcsec. LMC, SMC and the Galactic bulge have been monitored with this new setup from 1997 to 2000. Each field was observed every third night in I-band by OGLE-II, and every 11-th night in the V-band. OGLE-III had a $8K \times 8K$

pixel camera, made of 8 CCDs. Observations were performed towards SMC, LMC and the Galactic bulge [107] from June 2001 to May 2009. OGLE-IV is made of 32 E2V CCDs with $2K \times 4K$ pixels each and received its first light in September 2009.

DUO: Dark Unseen Objects. This search for microlensing towards the Galactic Center, also using the ESO-Schmidt telescope photographic plates digitized with the MAMA, was performed in 1994 [6].

MOA: Microlensing Observations in Astronomy. This team started microlensing searches with a 0.6m telescope located at mount John Observatory (New-Zealand), equipped with an array of 3×3 non-buttable $1K \times 1K$ CCDs [80]. Two different focal lengths were used during this first stage. The second camera had three $2K \times 4K$ pixels thinned SITe CCDs [119]. The team is now using a new 1.8m telescope, with ten $2K \times 4K$ pixels E2V CCDs [98] and it performs a real-time difference imaging analysis as described in [33].

SuperMACHO. From October 2001 to 2005, this collaboration used the 4m CTIO Blanco telescope during 150 half-nights, equipped with eight SITe $2K \times 4K$ CCDs and a $250nm$ passband VR filter, to monitor all star types in the LMC [93]. Considering the serious supernovæ contamination, complementary observations triggered through an alert system were used to identify microlensing events.

4 Analysis techniques

The data analysis of the surveys are all based on the same principles : Firstly, light curves (*i.e.* flux versus time curves) for cataloged stars or for emerging pixel clusters are extracted from the raw data, using automatic astrometric and photometric alignment procedures; secondly, each light curve is subjected to a microlensing search algorithm based on the expected characteristics of the events.

4.1 Photometry

Simple aperture photometry is not adapted for crowded fields. The microlensing pioneers have used or developed Point Spread Function (PSF) photometry techniques to extract the luminosity of each star in crowded fields ([20] and references therein for the photographic plates, [99] [21] for the CCD). A simultaneous fit of the PSF is performed on stars that are not completely separated. The following generation of microlensing teams have developed Difference Image Analysis techniques (DIA) [7] [115] [70] [33] that are very demanding in computing ressources, and are now usable thanks to the advances in computers. The base of this technique is the construction of the image difference between a current and a reference images. A convolution kernel is calculated and used to convolve the reference image to match the seeing of the current

image. The two images are then subtracted and the variability are searched from the study of the residuals. This technique has the advantage to make detectable the magnification of objects that are not detected when unmagnified.

4.2 Production of light-curves

Catalogs of objects are extracted from reference images, produced by the co-addition of series of the best quality images. For PSF photometry, the light-curves are produced after geometric and photometric alignment of current images on reference images. For DIA technique, a list of variable objects is extracted from the subtracted images and subsequently monitored in the other images.

4.3 Selection of microlensing candidates

The general philosophy for this discriminant analysis is as follows: if the starting point is a series of light-curves, the first stage consists in selecting the less stable objects, then to search for microlensing candidates through the topological characteristics of the expected light-curve. All analysis include a cleaning procedure, where bad quality images (taken under poor atmospheric conditions, with guiding problems...) are removed, sources with problematic environment (such as dead pixels or bright neighboring stars) are discarded from the reference catalog, and the identified aberrant measurements are suppressed. Various algorithms of discriminant analysis have been developed to pre-select light-curves with single positive fluctuations, visible in each color (in the case of multi-wavelength observations). Microlensing fits are performed on the pre-selected light-curves and the final selection is usually based on the fitted parameters.

The last selection stage is the background rejection and the residual background estimate. This stage has long suffered from being somewhat underestimated. Apart from the known experimental artifacts such as contamination by egrets or those induced by the SN1987A echoes [118], a few categories of objects that could mimic a microlensing event have been identified by the search teams over the years; the microlensing science would certainly benefit from a better understanding of these fakes:

- The so-called "blue bumpers" [12], bright blue variable stars that show recurrent bumps. Amongst them, Be type stars that are known to be unstable (case of the EROS1-1 candidate [27])

- Supernovæ that explode in galaxies behind the monitored target [17].

4.4 The efficiency control

The optical depth calculations require the knowledge of the detection efficiency as a function of t_E, averaged over the impact parameter space, over

the observation period and over the source apparent magnitudes and colors. This detection efficiency is defined as the ratio of the microlensing events that satisfy the selection requirements to the number of events with $u_0 < 1$ whose magnification reaches its maximum during the observing period. Its calculation needs the simulation of events in a domain of the parameter space that exceeds by a large amount the expected domain of sensitivity (in EROS, u_0 was generated up to 2, 1 $day < t_E < 900 \ days$, t_0 was generated from 150 days before the first observation to 150 days after the last one). The simplest technique to simulate microlensing-like light-curves consists in superimposing simulated events on measured light curves from an unbiased sub-sample of the monitored catalog. Events are simulated as point-source, point-lens, constant velocity microlensing events. This technique automatically takes into account the real time sequence, the source variabilities and the photometric systematic or accidental distortions that are preserved when combining with a simulated microlensing through rescaling procedures. The simulation of the microlensing in series of synthetic images (instead of light-curves) have also been made by [16] and [105], followed by the full photometric reduction and light-curve production. MOA used an intermediate technique of superimposing a microlensing effect on real subtracted images [104].

When the monitored population has a large distance dispersion, then the microlensing detection efficiency for a given stellar type depends on the distance, since it depends on the apparent magnitude. This makes the efficiency to be ultimately correlated with the optical depth itself. As the microlensing detection efficiency essentially depends on the *apparent* magnitude and possibly on the color, the mean optical depth up to a given magnitude (or for a given catalog) τ_{cat} is the concept that has to be used in the case of microlensing of populations with a wide distance distribution such as those belonging to the Galactic Spiral Arms [87]. Such a measured optical depth τ_{cat} can be compared with the predictions derived from a lens and source distribution model using expression (7), where the observed source distance distribution $\mathrm{d}n_S(D_S)/\mathrm{d}D_S$ corresponds to the cataloged sources (taking into account the star detection efficiency).

4.4.1 Blending

Due to source confusion, single apparent *cataloged objects* can be made of several *stars*. This fact, called blending, is one of the major sources of uncertainty for the optical depth determination in crowded fields, as it affects not only the microlensing detection efficiency but also the effective number of monitored sources N_{obs} that enters in expression (8) [44] [5] [116] [65]. When some blending is taking place, the reconstructed stellar flux contains contributions from more than one star. For this reason, the effective number of monitored sources N_{obs} that should enter in expression (8) is larger than the number of cataloged stars. Also, as only one of the components of the blend is magnified, this situation makes the reconstructed apparent magnification of the blend smaller than the real magnification of the lensed component. As a consequence, the
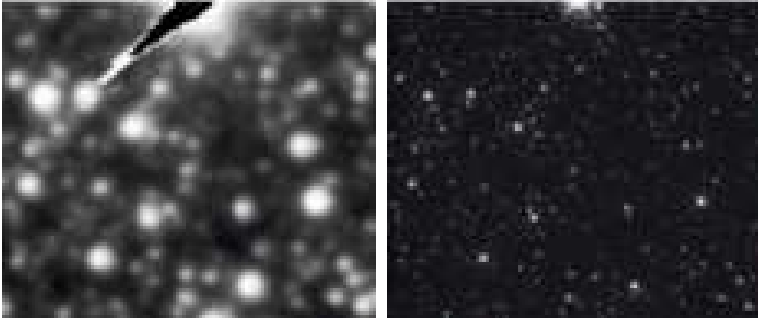
Fig. 2 *(left) The R_{EROS} composite image (used to detect the cataloged stars) and (right) the U6FQ1104B-HST image of the same sub-field towards gs201.*

detection efficiency appears smaller than for the unblended case. The impact of blending on the optical depth estimates has been studied by the observational teams using different approaches; as an example [3] [62] did a study based on synthetic images and on real images enriched with randomly located synthetic stars. In this type of simulation, it is usually assumed that there is no spatial correlation between the blend components and that the blend results only from a random coincidence. As the existence of correlation should increase the blending, this should be systematically checked and taken into account if necessary for the simulations. Other studies [17] [117] [87] compare HST images with the corresponding monitored subfields. For all these studies, the critical ingredient is the underlying luminosity function. Fig. 2 shows better than in words what is the blending in a Galactic plane field, and illustrates the relation between the (HST) luminosity function and the content of an EROS object. The HST images that are deeper by at least 2-3 magnitudes than the ordinary survey catalogs and have a PSF of $\sim 0.1''$ —10 times smaller than the terrestrial images— allow one to extract relevant statistical data in the underlying ingredients of the objects cataloged by the surveys.

A correction to the efficiency estimates is derived from these studies. There is some compensation between the loss of event-by-event efficiency and the gain in the effective number of monitored objects, that limits the impact on the optical depth estimates. Finally, the systematic uncertainty on the optical depth due to blending is generally estimated to be smaller than 10%. Decreasing this uncertainty needs a careful estimate of the blending corrections. The most simple way to minimize the impact of blending is to keep only microlensing of red giant (bright) stars. This option has been used by all the search teams towards the Galactic Center, and by EROS and OGLE towards the LMC.

4.4.2 The efficiency uncertainties due to complex events

The efficiency estimates are based on the simulation of simple microlensing events. It has been estimated that about 10% of the real microlensing events

have a more complex evolution such as a double lens configuration or a parallax effect [54]. In the later case, the correction is usually small, but in the first (rare) case, the mean detection efficiency may be seriously affected by the distorted shape of the light-curve [54]. The impact of this detection modification is sometimes accounted for as an extra-uncertainty of $\sim 10\%$ on the detection efficiency.

4.5 Complementary observations and statistical tests

These *a posteriori* tests are crucial not only to check and improve the background rejection, but also to gain confidence in the statistical distributions. The first microlensing candidates have been investigated in details through complementary photometric and spectroscopic measurements. A non negligible fraction of the early candidates (with low signal to noise) has been rejected after publication because of the late discovery of anomalies such as repetition of bumps (*e.g.* the so-called "blue-bumpers" [12]) or baseline variability [22]. In connection with optical depth studies, systematic statistical tests are performed on the populations of detected microlensing candidates to check that the impact parameter u_0 and the maximum magnification time t_0 distributions —with uniform prior— are only biased by the detection efficiencies, and that this population is representative of the monitored population after correcting for the detection efficiencies.

5 Some limitations and difficulties in the optical depth determination and future improvements

5.1 Statistical limitations

The impact of poor statistics is worsen by the dispersion of the microlensing event durations; since the variability of the durations induces a strong variability of the individual contributions to the optical depth, the statistical uncertainties on this parameter are indeed larger than expected from Poisson statistics. This is taken into account by the search teams by using the procedure described in [64].

One of the statistical limitations in the microlensing surveys is the available number of sources that can be monitored. As an example, optical depth measurements towards obscured regions of the Galactic plane are very strongly limited by the visibility of the sources. The only way to improve the situation is to make infrared surveys [56]. The VVV (VISTA Variables in the Via Lactea) program [114], one of the VISTA[3] [113] large survey programs, aims at searching for variabilities towards the Galactic plane and should have a major impact for the microlensing searches towards the dusty regions.

---

[3] Visible and Infrared Survey Telescope for Astronomy

Another statistical limitation —more difficult to overcome— comes from the weakness of the signal itself; more exposure ($N_{obs} \times \Delta T_{obs}$) is needed to compensate for the low microlensing rate towards the Magellanic Clouds. SuperMACHO [93] which monitored the largest possible number of stars within the LMC was specifically devoted to this search.

5.2 Information from simple events

The ordinary microlensing events provide little physical information on the lens configuration. Any technique improving the photometric accuracy through the use of larger telescopes or by achieving high sampling rates increases the chance to get some extra-information by the detection of small deviations with respect to the simple microlensing light-curve. International networks of relatively small telescopes linked to the alert systems of surveys like PLANET[4] [85] MicroFUN[5] [77] or MINDSTEp[6] [78] have developed the second approach.

The LSST[7] project [72] will certainly dramatically change the landscape for the photometric accuracy, as the telescope has an equivalent diameter of 6.5m. Tens of thousands of events should be detected each year with a sampling rate of once every few nights. Considering the photometric accuracy, parallax and extended source effects will often be detectable and improve the knowledge of the lens configuration; but high sampling networks will be needed in the case of very fast variations during the caustic crossing of double lens events.

5.3 Limitation from the knowledge of the source distance distribution

The Magellanic Clouds are stellar populations located at well defined distances. Therefore, the allowed parameter space of an observed lens configuration is less extended than when the source distance is poorly known. The distance distribution of the Galactic bulge population is wider, but the relative uncertainty on the bright source's positions is less than 10% [82]. This uncertainty does not have a strong impact on the optical depth estimates. In contrast, monitored sources at large Galactic longitude can span a wide range of distances (see Sect. 6.2). The interpretation of the mean optical depths requires either a good knowledge of the source distance distribution (through complementary observations such as spectroscopy) or a model that allows the simulation of the survey catalogs and to predict the mean optical depths [87].

---

[4] Probing Lensing Anomalies NETwork
[5] Microlensing Follow-Up Network
[6] Microlensing Network for the Detection of Small Terrestrial Exoplanets
[7] Large Synoptic Survey Telescope

6 Review of results

6.1 Galactic model

We describe below the model and the parameters of one of the simplest Galactic models, that is commonly used for the optical depth interpretations. To facilitate the comparisons, we will interpret all the optical depth results and some event duration distributions within this framework, and briefly mention the alternatives in the subsequent discussion. The model includes a central bulge, a thin disk, a hypothetical thick disk and a halo; since the exact morphology of the Galactic Spiral Arms (GSA) is yet unknown [49], no spiral arm features have been included in the model. The parameters we use here are summarized in Table 2.

– **The observer position and velocity:** To calculate the optical depths and duration distributions within the Galactic plane, one needs to take into account the position of the Sun with respect to the disk ($15.5 \pm 3\,pc$ above the median plane, according to [63]) and the peculiar solar motion with respect to the Local Standard of Rest [39]:

$$v_{\odot R} = 10.0,\ v_{\odot \theta} = 5.3,\ v_{\odot z} = 7.2\ \ (\mathrm{km s^{-1}}). \qquad (10)$$

– **The Galactic halo:** Many models of the Galactic halo have been tested to interpret the observations; from the simple "standard" spherical halo to flattened halo. Discussions can be found in [31] [47] [53], and the corresponding predicted optical depth maps can be found in [50]. We will only consider here the so-called S-model [12] that allows the easiest comparisons and combinations between the various published results towards LMC and SMC. This spherical halo is considered as isotropic and isothermal with a density distribution given in spherical coordinates by :

$$\rho_H(r) = \rho_{h\odot} \frac{R_\odot^2 + R_c^2}{r^2 + R_c^2}\ , \qquad (11)$$

where $\rho_{h\odot}$ is the local halo density, $R_\odot$ is the Galactocentric radius of the sun, R_c is the halo "core radius" and r is the Galactocentric radius. A Maxwellian distribution is assumed for the velocities with a one-dimensional dispersion σ_{1D}. Usually authors consider mono-mass distributions for the lenses when simulating microlensing.

– **The Galactic disks:** The disk densities are modeled by a double exponential expressed in cylindrical coordinates:

$$\rho_D(R, z) = \frac{\Sigma_\odot}{2H} \exp\left(\frac{-(R - R_\odot)}{h}\right) \exp\left(\frac{-|z|}{H}\right)\ , \qquad (12)$$

where $\Sigma_\odot$ is the column density of the disk at the Sun position, H the disk height scale and h its length scale. A thick disk has been discussed as a possible component of the Galactic structure [58] [89] [40] [41] [87], for the interpretation of the optical depth towards LMC/SMC and far from the

Table 2 Parameters of the Galactic model.

		Thin	Thick
	$R_\odot$ (kpc)	8.5	
Disks	$\Sigma_\odot$ ($M_\odot \mathrm{pc}^{-2}$)	50.	35.
	H (kpc)	0.325	1.0
	h (kpc)	3.5	3.5
	$M_{thin}(\times 10^{10} M_\odot)$	4.3	3.1
	σ_r ($km\ s^{-1}$)	34.	51.
	σ_θ ($km\ s^{-1}$)	28.	38.
	σ_z ($km\ s^{-1}$)	20.	35.
Bulge	a (kpc)	1.49	
	b (kpc)	0.58	
	c (kpc)	0.40	
	Inclination Φ	45°	
	$M_B(\times 10^{10} M_\odot)$	1.7	
	σ_{bulge} ($km\ s^{-1}$)	110.	
Halo S-model	$\rho_{h\odot}$ ($M_\odot \mathrm{pc}^{-3}$)	0.0078	
	R_c (kpc)	5.0	
	σ_{1D} ($km.s^{-1}$)	155.	
	$M\ in$ 60 kpc ($10^{10} M_\odot$)	40	
Predictions	$\rho_\odot$ ($M_\odot \mathrm{pc}^{-3}$)	0.085	0.098
	$V_{rot}\ at\ sun$ (km s^{-1})	211	222
	τ_{LMC}	4.7×10^{-7}	
	τ_{SMC}	6.58×10^{-7}	

Galactic center. The kinematics of these disks involves a global rotation given by [34]

$$V_{rot}(r) = V_{rot,\odot} \times \left[1.00762 \left(\frac{r}{R_\odot} \right)^{0.0394} + 0.00712 \right] , \qquad (13)$$

where $V_{rot,\odot} = 220$ km/s [34], and an anisotropic Gaussian peculiar velocity distribution, characterized by the velocity dispersions of Table 2. The mass function for the lenses is taken from [57] for both the thin disk and the bulge.

– **The Galactic bulge:** The density distribution for the bulge - a bar-like triaxial model - is taken from [47] model G2, given in Cartesian coordinates:

$$\rho_B = \frac{M_B}{6.57\pi abc} e^{-r^2/2} , \ \ r^4 = \left[\left(\frac{x}{a} \right)^2 + \left(\frac{y}{b} \right)^2 \right]^2 + \frac{z^4}{c^4} , \qquad (14)$$

where M_B is the bulge mass, and a, b, c the length scale factors. The inclination of the bar [101] differs with the authors (from $\sim 14°$ according to [53] to 45° according to [62] and [84]). The transverse velocity distribution of the bulge stars is given by

$$f_T(v_T) = \frac{1}{\sigma_{bulge}^2} v_T \exp \left(-\frac{v_T^2}{2\sigma_{bulge}^2} \right) . \qquad (15)$$
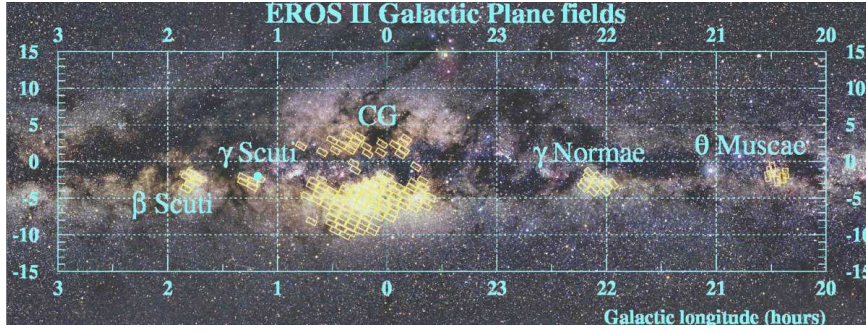
Fig. 3 *View of the Galactic plane and fields monitored by EROS.*

6.2 Results towards the Galactic plane

Figure 3 shows the fields monitored by EROS towards the Galactic plane. The fields monitored by MACHO, OGLE and MOA are all included within the bright zones of the Galactic center. MACHO also monitored fields close to $\gamma Scuti$ ($l \sim 18°$) and OGLE monitored fields at $l \sim -20°$ and $l \sim -30°$, but only EROS published optical depth measurements far from the Galactic Center ($|l| > 8°$). More than 4000 events have been detected towards the Galactic bulge (but only a fraction of them have been used to obtain optical depths under controlled efficiency), and 27 towards the Galactic Spiral Arms (22 used for optical depth determination). The interpretation of the optical depth measurements is somewhat complicated by the limited knowledge of the lensed source distances. Indeed, the optical depth estimated for the full sample of detected stars or with DIA analysis is the average over all the stars across the lines of sight of the GC. The optical depths towards the spiral arms also correspond to average values. The uncertainty on the source distances is reduced towards the Galactic center by selecting the clump giant stars, with the triple advantage to monitor a well located population ($D_S = 8.5\ kpc \pm 10\%$), less affected by blending problems, and benefiting from a better photometric accuracy because of the brightness of the sources. The sources monitored towards GSA span a wide range of distances (± 5 kpc) and their mean distance —estimated to be $7 \pm 1\ kpc$— is also somewhat uncertain [87]. In the latter case, the measured optical depth towards the monitored population corresponds to expression (7) where $\mathrm{d}n_S(D_S)/\mathrm{d}D_S$ is the distance distribution of the *monitored* stars, corresponding to the true distribution distorted by the star detection efficiency. Because of this limited knowledge of the source distances, the results are compared with optical depth estimates at various distances. The following optical depth measurements are summarized in Fig. 4 (here $< t_{\mathrm{E}} >$ is corrected for the detection efficiencies):

reference	sea-sons	field $deg.^2$	stars analyzed	events for τ	$\bar{l}^\circ, \bar{b}^\circ$	$<\tau>_{bulge}$ $\times 10^6$	$<t_E>$ corrected
OGLE [112]	2	0.81	all	9	$\pm 5, -3.5$	3.3 ± 1.2	
MACHO [11]	1	12.	all	45	2.55, 3.64	$3.9^{+1.8}_{-1.2}$	
MACHO [16]	3	4.	all/DIA	99	$2.68, -3.35$	$3.23^{+0.52}_{-0.50}$	
EROS [3]	3	15.	bright	16	$2.5, -4.0$	0.94 ± 0.29	
MOA [104]	1	18.	all/DIA	28	$4.2, -3.4$	$3.36^{+1.11}_{-0.81}$	
MACHO [86]	7	4.5	bright	62	$1.5, -2.68$	$2.17^{+0.47}_{-0.38}$	21.6 ± 3
OGLE [105]	4	5.	bright	32	$1.16, -2.75$	$2.55^{+0.57}_{-0.46}$	28.1 ± 4.3
EROS [62]	7	66.	bright	120	GC map		28.3 ± 2.8
EROS [87]	7	20.1	all	22	GSA map		$48. \pm 9.$

Many of these measurements are correlated because of the large overlap between the survey's exposures ($N_{obs} \times \Delta T_{obs}$). Merging these results would require a close collaboration between the authors of these surveys.

The variation with the latitude deduced from the largest sample (EROS) is well fitted by

$$\tau/10^{-6} = (1.62 \pm 0.23)\exp[-a(|b| - 3^\circ)], \text{ with } a = (0.43 \pm 0.16)\deg^{-1} . \quad (16)$$

This fit agrees with the latest results of MACHO [86] and OGLE-II [105] that use only bright stars, and with the Galactic models of [50] and [32]. The estimates deduced from DIA analysis as well as from searches using all the detected stars correspond to average optical depth along the line of sight of the GC. For a relevant comparison with the optical depth involving bright stars only that are all supposed to be close to the Galactic center, we plot in Fig. 4 the optical depth τ_{bulge} corrected for the parasitic disk-disk lensing. Nevertheless, these "all star measurements" seem to be somewhat systematically larger than the measurements restricted to bright stars. The corrections for disk-disk lensing may be a little too large, or the impact of disk bright stars may have been underestimated.

A local excess of optical depth has been reported by [86] with a 2σ statistical significance, but no conclusive evidence for clustering of events was found. The measured τ_{GSA} agrees with the predictions of the simplest Galactic model (Fig. 4 down), providing no evidence for a thick disk.

Detailed maps of the expected microlensing optical depth are now available [69] for the interpretation of the available and future observations towards the Galactic bulge. They provide optical depths up to a given magnitude.

The evaluation of the efficiencies needed by the optical depth determinations allows us to correct any distribution in order to extract the prior distributions. This has been used firstly to check the statistical properties of the events as already mentioned in Sect. 4.5, and then to obtain their prior t_E distributions. These t_E distributions given by the three collaborations have been recently analyzed by [37] to constrain the slope of the Galactic Bulge mass function ($\sim m^{-\alpha}$) in the main sequence (MS) range; the result from the MACHO data set ($\alpha_{MS} = 1.7 \pm 0.5$) was found compatible with the numbers deduced from the OGLE and EROS data sets, and also in agreement with previous estimates [122].
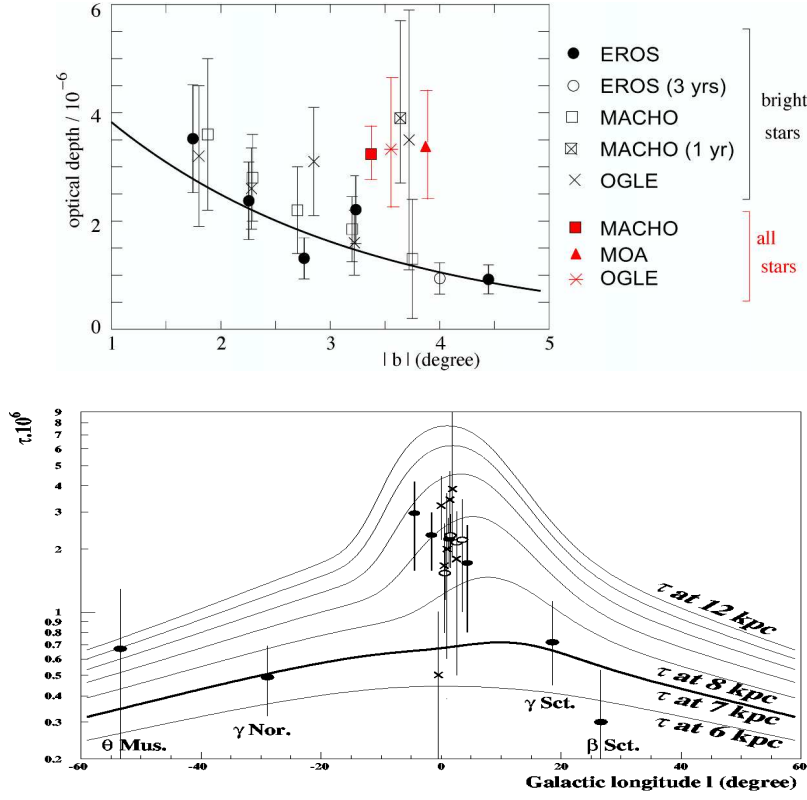
Fig. 4 *(up) The measured optical depth in the Galactic plane as a function of the absolute Galactic latitude |b|. The line shows the fit (16). (down) The optical depth as a function of Galactic longitude. Results at large longitude |l| > 8° come from the specific EROS GSA search at b ∼ −2.5°. Results around longitude zero (MACHO: open circles, EROS: filled circles, OGLE: crosses) come from the Galactic center searches at |b| ∼ 2.5°. The lines show the predicted optical depths as a function of latitude at 6,7 (thick line), 8, 9, 10, 11 and 12 kpc (from lowest to highest curve) at b = −2.5°, according to the model described in Sect. 6.1. The measured optical depth around l = 0° are compatible with the expected optical depth at 8.5 kpc; the best estimated mean distance for the sources in the Galactic Spiral Arms is confirmed to be 7 kpc.*

As a conclusion regarding the Galactic plane directions, there is now a satisfactory agreement between the optical depths and the efficiency corrected duration distributions obtained by the various teams. This agreement, as well as the agreement with the Galactic models, give confidence in the reliability of the technique, which is necessary to address the more controversial subject of the microlensing towards the Magellanic Clouds.
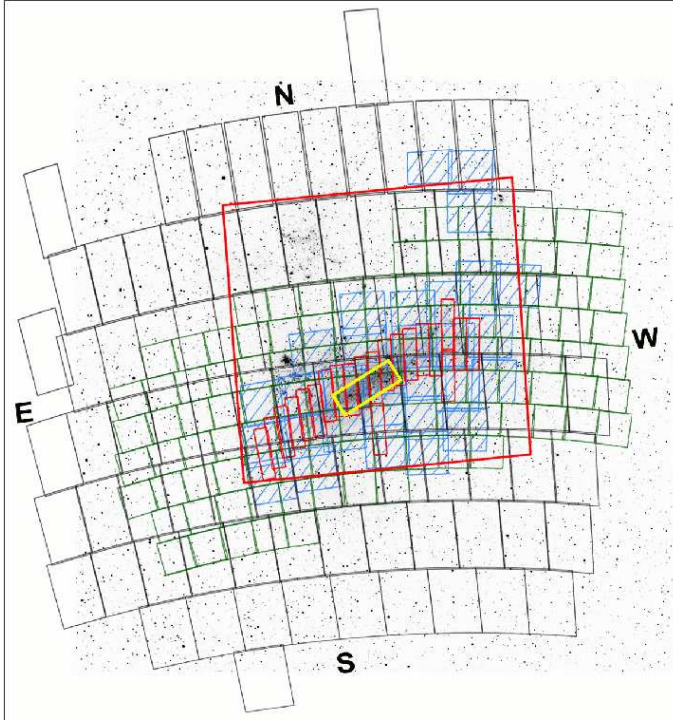
Fig. 5 *Approximate positions of the monitored LMC fields. The red rectangles (resp. green squares) show the OGLE-II (resp. OGLE-III) fields, the blue dashed squares show the MACHO fields, the red large square is the EROS1-plate field, the small yellow rectangle within the LMC-bar indicates the EROS1-CCD field, and the black rectangles show the EROS-2 fields.*

6.3 Results towards the Magellanic clouds

Figure 5 shows the fields monitored by the different teams towards LMC. The surveys of SMC are much more limited because of the size of this target. The optical depths towards these directions have been studied by MACHO, EROS and OGLE. Detection of candidates has also been reported by the MOA collaboration [80], but without optical depth estimates.

The main result from the LMC/SMC surveys is that compact objects of mass within $[10^{-7}, 10] \times M_\odot$ interval are not a major component of the hidden Galactic mass (Fig. 6).

Light objects ($< 10^{-1}M_\odot$) in the Galactic halo were clearly ruled out as early as 1997 by EROS1 [90] which did not find any short time-scale events (with $t_E < 1$ *day*). Heavy objects (1 to $30M_\odot$) contribution to the Galactic halo was also seriously constrained as soon as 2001 by MACHO [19].

The contribution of medium mass objects to the halo *has been* a more controversial subject, as background sources as well as self-lensing contributions
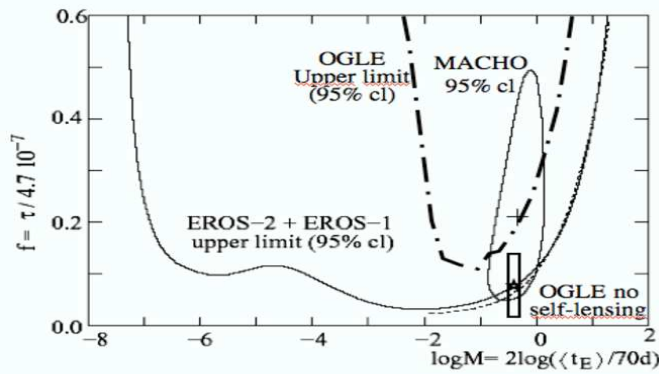
Fig. 6 *Published constraints on the fraction f of the standard spherical Galactic halo made of massive compact objects as a function of their mass M. The solid line labeled EROS shows the EROS upper limit [106], based on the combination of the EROS1 results with the LMC EROS2 results. The dotted (incomplete) line takes into account the SMC search direction, assuming that the observed candidate belongs to the halo. The OGLE upper limit [117] is shown in dashed-dotted line. The closed domain is the 95% CL contour for the f value claimed by MACHO and the star surrounded by the small rectangle shows the contribution of the 2 OGLE events, assuming that they belong to the halo.*

[95] [96] have complicated the data analysis and its interpretation. The MA-CHO collaboration has published non-zero halo signal estimates towards the densest part of the LMC, but EROS did not find indisputable events within its sub-sample of bright stars in its wider LMC search field, and has only published upper limits on the halo contribution. To illustrate some of the difficulties of the LMC analyses, we have to mention that three of the MACHO [30] and ten of the EROS [106] LMC/SMC early published candidates have been discarded as viable microlensing events because of a significant loss of the signal to noise ratio from longer light-curves or because of the detection of a second bump (as late as 8 years later [73]).

6.3.1 Exclusion limits on the Galactic halo

Four results are mutually compatible:

– the EROS upper limit [106],
– the MACHO high-mass upper limit [19],
– the most recent OGLE-II upper limit [117],
– and the first combination of data from different teams [14] (hereafter called EROS1-CCD+MACHO) obtained with the EROS1-CCD high sampled data (20 minutes) taken in 1991-95 with the 16 CCD camera [90] [91] and with the MACHO-2year short events search in 1992-94 through a spike analysis [10].

The upper limit, considered as a function $f_\delta(M)$, is the maximum contribution of objects of mass M to the S-model halo optical depth, expressed in

fraction f. The maximum contribution f_F of a population with a (normalized) mass distribution $F(m)$ different than a Dirac function $\delta(m - M)$, is given by

$$f_F = \left[\int \frac{F(m)}{f_\delta(M)(m)} \mathrm{d}m \right]^{-1}. \qquad (17)$$

We can combine the "zero event" analysis to obtain a stronger constraint towards LMC. Including the non-zero event measurements from the SMC or from the OGLE-II [117] analysis in such a combination would need a specific collaborative work, since the corresponding exclusion limits depend on the expected background of non-halo events in each survey (see below).

Combination of the limits on the low mass side: The simplest way to combine the 95% exclusion results is to consider the lower envelope of the exclusion curves from all the null analyses. A more sophisticated technique would be to calculate the exclusion limits by adding the signals expected by each analysis, taking into account only once those objects that are monitored simultaneously by several surveys. Figure 7 (top panel) shows the numbers of events expected from the S-model halo lenses for each of the "zero event" experiments (EROS1-CCD, EROS1-plates, EROS2, EROS1-CCD+MACHO, MACHO high-mass) [8]. A complete combination, following [14] would need a close collaboration between the teams involved. Nevertheless, a simple combination can be made:

- let $n_{EROS1-plates}(M)$, $n_{EROS1-CCD+MACHO}(M)$ and $n_{EROS2}(M)$ be the expected numbers of events as a function of the lens mass M for the corresponding analysis;
- since the EROS1-plates data overlap with the MACHO-2year observations, they overlap with the combined EROS1-CCD+MACHO analysis. Therefore, the total number of expected events from the EROS1-plates plus the EROS1-CCD+MACHO analysis is not the sum of the expected numbers but it is at least larger than $n_{EROS1-plates}(M)$ and $n_{EROS1-CCD+MACHO}(M)$ (grey dashed line in Fig. 7-top panel);
- since the data sets of the EROS1-plates and of the combined EROS1-CCD+MACHO analysis do not overlap with the EROS2 analysis the function

$$n_{EROS2}(M) + max[n_{EROS1-plates}(M), n_{EROS1-CCD+MACHO}(M)] \quad (18)$$

represents a minimum for the total number of events expected from all these analyses (thick line in Fig. 7-top panel).

Using this combination allows us to improve the exclusion limit between 10^{-5} and $10^{-4} M_\odot$ with respect to the envelope of the EROS/MACHO upper limits (Fig. 7 (bottom panel)).

---

[8] in these experiments, the zero event observed are the very final numbers after rejection from complementary observations, as discussed just before this sub-section.
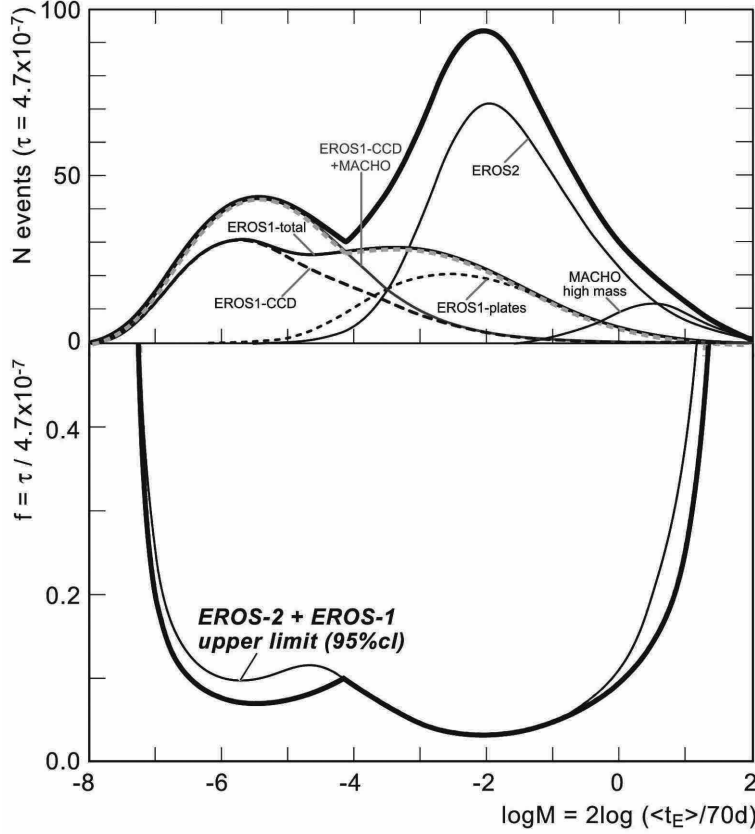
Fig. 7 *The top panel shows the number of expected events towards LMC as a function of the lens mass M for the S-model. The EROS1-total line shows the sum of the expectations from the CCD-camera and from the plates (dashed lines). The MACHO-high mass line corresponds to the "zero event" high mass search. The EROS1-CCD+MACHO line (blue) is the combined result from the EROS1 CCD-camera and the MACHO 2 year analysis. The grey dashed line is the envelope of the EROS1-total and the EROS1-CCD+MACHO lines. The final combination (thick line) is the sum of EROS2, of the grey dashed line and of half of the MACHO-high mass expectations (see text). In the lower panel, the thick line shows the combined* 95% *CL upper limit on* $f = \tau_{LMC}/4.7 \times 10^{-7}$ *based on no observed events. The thin line is the EROS1+EROS2 LMC limit.*

Combination of the limits on the high mass side: Another combination can be made on the high mass side with the MACHO high-mass "zero event" analysis [19] and the EROS results [106]; the MACHO search did not overlap with the EROS searches for more than 3 years (1994-96), in the middle of the MACHO 5.7 year analysed observations; therefore one can conservatively add half of the total published expectations from the MACHO high-mass search to the expectations from the other "zero-signal" searches. This is conservative as the detection efficiency —specifically for long duration microlensing— is

better for events that have their maximum in the middle of the observation period.

The OGLE upper limit: No simple combination can be made with the OGLE-II results [117], as their field and observation epoch are entirely covered by the EROS2 program. As for MACHO, the OGLE-II catalog of monitored stars contains fainter stars than the EROS2 catalog, and a combination of these results could potentially improve the limits but would need a close collaboration between the teams. Such a combination would also be much more complicated, as the OGLE analysis is not a "zero-signal" analysis; like the one SMC-event found by EROS and MACHO [2] [13], the 2 events found by OGLE-II cannot be unambiguously affected to self-lensing. Because of the existence of these events, according to standard statistics, the OGLE-II limit should not be estimated by considering that 3 events correspond to the 95% CL excluded mean value; indeed, the 95% CL upper limit on the mean signal $\bar{S}$ contaminated by a background known by its expected mean value $\bar{B}$, were $S + B$ follows a Poisson law, is not 3 when the observed number is equal to $\bar{B}$. In the present case, if one assumes that $\bar{B} = 2$ (which is probably a maximum according to [117] [61] [17] [29] and [74]), then following [52], the 95% upper limit when 2 events are observed is $\bar{S} < 4.72$. This limit would be lower only if $\bar{B} > 2$. If $\bar{B} = 2$, the OGLE upper limit on the halo component should be corrected by a factor $4.72/3 = 1.57$, but this needs to be finalized using the exact value of $\bar{B}$. The statistical procedure described in [20] could also be used for the OGLE-II non-zero event analysis.

6.4 The Galactic halo

6.4.1 The apparent discrepancies towards the LMC

We can quantify the incompatibility between the MACHO results from [12] and [17] and the EROS results [106]. The 13 observed events by MACHO in [17] correspond to a fraction $f_{MACHO} = 0.21$ of the S-model halo; The MACHO collaboration has estimated that at least 9.6 of these events should be due to hidden baryonic matter (Milky-Way or LMC halo). This corresponds to $9.6/f_{MACHO} = 45.7$ events expected with a full S-model halo entirely made of objects of mass $0.6M_\odot$. For the same mass, about $39 \times f_{MACHO} = 8.2$ events are expected in the EROS1+EROS2 LMC data while zero were observed. For a mass $0.9M_\odot$, which is 1σ larger than the central MACHO value, $30 \times f_{MACHO} = 6.3$ events were expected in the EROS data. Assuming an optical depth dominated by the Galactic halo and no correlation between the data sets, the EROS and MACHO measurements are statistically incompatible. The correlations due to the (actually small) overlap between the data sets makes this incompatibility worse.

There are considerable differences between the EROS, MACHO and OGLE data sets that may —at least partially— solve the apparent conflict. Generally speaking, MACHO uses faint stars in dense fields (1.2×10^7 stars over 14 $deg.^2$)

while EROS2 uses bright stars in sparse fields (0.7×10^7 stars over 90 $deg.^2$). As a consequence of the use of faint stars, only two of the 17 MACHO (set B) candidates were sufficiently bright to be compared to the EROS bright sample; as the corresponding events occurred before the EROS data taking, there is no evidence for a malfunctionning experimental setup during one of the surveys. The use of dense fields by the MACHO group also suggests that the higher MACHO optical depth may be due, in part, to self-lensing in the inner parts of the LMC [61]. The contamination of irregular variable objects faking microlensing in low photometric resolution events could also be stronger in the sample of faint stars used by MACHO. As already mentioned, another difficulty when using faint source stars originates in the blending effects that complicate the optical depth calculations.

6.4.2 The SMC case

In the framework of the S-model halo, the EROS upper limit on the halo fraction from the combined LMC/SMC studies in [4] and [106] assumes that $\tau_{SMC-halo} = 1.4 \times \tau_{LMC-halo}$; this would be larger with a flattened halo or a thick disk. The dotted line in Fig. 6 shows the small impact of the SMC measurements according to this model. Even though the impact on the optical depth estimates seems limited, the compatibility of the SMC microlensing events population with the LMC one is the subject of an interesting debate. The long durations of the four SMC events published in the 5-year search of EROS [4] is found to be incompatible with the t_E distribution of the MACHO LMC events [17], and make these events more compatible with unidentified variable-type stars or with SMC-self-lensing. This issue is discussed by [97].

Because of their long duration, a fair fraction of the SMC events could benefit from complementary studies, thus providing indications on the lens population. The first event towards SMC (MACHO-SMC-97-1/EROS-SMC1) was discovered in 1997 and observed by both MACHO [13] and EROS [83]. Thanks to its long duration ($t_E = 123\,days$) and its brightness, a parallax analysis was performed on the light-curve, and from the absence of measurable distorsion, it was concluded that the lens probably belonged to the SMC itself. This interpretation was confirmed from the Spectroscopy of the lensed star [97]. The second event discovered towards SMC (MACHO-SMC-98-1) was the first event from the Magellanic Clouds to benefit from an intensive international collaboration between MACHO [15], EROS [1], PLANET [8], OGLE [109] and MPS[9] [94] collaborations on 18 June 1998, as it was early detected by MACHO as a binary-lens microlensing event. The common conclusion from the different survey teams was that the proper motion of the lens was consistent with the lens beeing within the SMC rather than in the Galactic plane or halo. But at least one SMC-event, OGLE-2005-SMC-001, measured both from Earth and from space [46], had a parallax estimate such that the probability for the lens to belong to the halo was 20 times larger than to belong to the SMC. The two

[9] Microlensing Planet Search

later events do not enter in any optical depth calculation, and they are only mentioned here to illustrate the problem of the lens location. Unfortunately, the very small statistics limits the interpretations, but we can conclude that the SMC lens population is probably not dominated by the Galactic halo, and is certainly different from the LMC lens population.

6.4.3 A synthesis attempt: halo versus local structures

Taking all the observational results at their face value, we may conclude that the initial hypothesis of an optical depth dominated by the Galactic halo — almost uniform through all the monitored LMC fields and 1.4 times larger towards SMC— is wrong, because it cannot explain the EROS-MACHO differences nor the LMC-SMC differences.

As the results found by the teams are mutually compatible towards the Galactic plane directions (Sect. 6.2), the falseness of this hypothesis should now be favored rather than the eventuality of wrong measurements.

Abandoning the original microlensing survey paradigm of a dominant halo allows one to explain the variety of the observations by the large differences in the monitored fields. Fig. 5 supports this view. If —as suggested by their small contribution to the halo— one assumes that lenses do not trace the Galactic halo hidden matter, then the apparent discrepancy between the surveys can be understood by considering local structures inducing self-lensing; such structures (populations of foreground lenses as well as populations of background sources [18]) may be responsible for the variability of the mean optical depth with the monitored fields. Nevertheless, a convincing proof of the existence of such structures is still to be provided. One of the aims of the current and next generations of microlensing surveys towards LMC (like SuperMACHO) is to improve the knowledge of the lens populations, and specifically their location.

For a pertinent synthesis, it seems that the total optical depth —understood as an *average* over the monitored fields— is the perennial observable that will allow the building of contour maps of the massive compact object spatial distribution. The following numbers have to be *imperatively* associated with the corresponding fields:

- $\tau_{LMC-MACHO} = (1.0 \pm 0.3) \times 10^{-7}$, after revision by [30]. There have been some controversy on the MACHO optical depth estimates. The first estimate from [12] was clearly much too high ($\tau = 2.9^{+1.4}_{-0.9} \times 10^{-7}$). This result was seriously downsized to $\tau = 1.2^{+0.4}_{-0.3} \times 10^{-7}$ after the analysis of 5.7 years of data [17]. MACHO collaborators and outsiders have revised/disputed the later result; [30] took into account known contamination of the signal by non-microlensing variabilities and published a revised optical depth of $\tau = (1.0 \pm 0.3) \times 10^{-7}$. [28] and [29] have re-analized the publicly available MACHO light-curves with a neural network system and estimated a number of contaminants larger than the one quoted in the original MACHO paper. They conclude that $\tau_{LMC-MACHO} = (0.4 \pm 0.1) \times 10^{-7}$. A controversy followed ([60] and [51]).

- $\tau_{LMC-EROS} < 0.36 \times 10^{-7}$ (95% CL).
- $\tau_{LMC-OGLE} = (0.43 \pm 0.33) \times 10^{-7}$ is the total measured optical depth (taking into account 2 observed events).

The distributions of event durations (except for EROS which has no event) have also been used by several authors to refine the interpretations. For example, a detailed study of the consequences of the MACHO results was performed in [68], which takes into account the optical depths, rates and durations expected from several Galactic structures (thick disk, spheroid) through the mass moment method [42] [43], and concluded that at least 3 of the observed microlensing events were due to LMC lenses, but that the others were probably due to other Galactic structures. More recently [36] concluded that up to about half of the MACHO events could be attributed to the LMC dark matter halo instead of the Milky-Way dark halo. Calchi Novati *et al.* [38] also conclude from their rate and durations that the 2 events reported by OGLE-II are perfectly compatible with the expectation from known lenses (*i.e.* not dark), dominated by the LMC self-lensing.

Conclusion

A substantial contribution of compact objects to a standard halo is now clearly excluded. Compact objects belonging to a flattened halo or a thick disk are also seriously limited by observations both towards SMC and GSA. Wether or not there is a small dark matter component under the form of compact objects is still an open question.

7 The future of the optical depth studies

Several authors have investigated the possibility to systematically use complementary observations —instead of occasionnally as currently done— to look for non-standard features. Systematic searches for parallax effects towards LMC have been examined by [88] based on the use of the ESO-NTT telescope, and by [103] using measurements by the ESO-VLT or by the Hubble Space Telescope on strongly magnified sources. Such follow up measurements would increase the information about the events and help to localize the lens populations. Accurate mapping of the optical depth is another way to improve the knowledge on these populations and to measure the self-lensing contributions. Microlensing searches that address this question are currently running or about to observe: SuperMACHO [93], OGLE-III and IV [107] and the infrared VVV project [114] using VISTA facility, should renew this scientific domain within the next few years. The LSST program will certainly dominate the following decade of microlensing studies as a microlensing factory, possibly with contributions from spatial missions like GAIA.

References

1. Afonso C., Alard J.-N., Albert J.-N. *et al.* (EROS Coll.), 1998, A&A, 337, L17
2. Afonso C., Alard C., Albert J.-N. *et al.* (EROS Coll.), 1999, A&A, 344, L63
3. Afonso C., Alard C., Albert J.-N. *et al.* (EROS Coll.), 2003, A&A, 404, 145
4. Afonso C., Albert J-N., Andersen J. et al., 2003, A&A, 400,951
5. Alard C., 1997, A&A 321, 424
6. Alard, C., and Guibert, J. 1997, A&A, 326, 1
7. Alard, C. and Lupton, R. 1998, ApJ 503, 325
8. Albrow M.D., Beaulieu J.-P., Caldwell J.A.R., et al., 1999, ApJ, 512, 672
9. Alcock C., Akerlof C.W., Allsman R.A. *et al.* (MACHO Coll.), 1993, Nature, 365, 621
10. Alcock C., Allsman R. A.,Alves D. *et al.* (MACHO Coll.), 1996, ApJ 471, 774
11. Alcock C., Allsman R.A., Alves D. *et al.* (MACHO Coll.), 1997, ApJ 479, 119.
12. Alcock C., Allsman R. A., Alves D. *et al.* (MACHO Coll.), 1997, ApJ, 486, 697
13. Alcock, C., Allsman, R. A., Alves D., *et al.* (MACHO Coll.), 1997, ApJ, 491, L11
14. Alcock C., Allsman R. A., Alves D. *et al.* (EROS & MACHO Coll.), 1998, ApJ, 499, L9
15. Alcock C., Allsman R.A., Alves D. *et al.* (MACHO Coll.), 1999, ApJ 518, 44.
16. Alcock C., Allsman R.A., Alves D. *et al.*, 2000, ApJ 541, 734
17. Alcock C., Allsman R.A., Alves D. *et al.*, 2000, ApJ, 542, 281
18. Alcock C., Allsman R.A., Alves D. *et al.*, 2000, ApJ, 552, 582
19. Alcock C., Allsman R.A., Alves D. *et al.*, 2001, ApJ, 550, L169
20. Ansari R., Cavalier F., Moniez M. *et al.* (EROS Coll.), 1996, A&A 314, 94
21. Ansari R., 1996, Vistas in Astronomy, Vol. 40, No 4, 519-530
22. Ansari R., Cavalier F., Couchot F. *et al.* (EROS Coll.), 1995, A&A 299, L21
23. Arnaud M., Aubourg E., Bareyre P. *et al.* 1994, Exp. Ast., 4, 265 (I) & 279 (II)
24. Aubourg É., Bareyre P., Bréhin S. *et al.* (EROS Coll.), 1993, Nature, 365, 623
25. Aubourg E., Bareyre P., Bréhin S. *et al.* 1993, ESO-Messenger, 72, 20
26. Bauer F. *et al.* (EROS coll.) 1997, proc. of the "optical Detectors for Astronomy" workshop, ESO.
27. Beaulieu J-P. Ferlet R., Grison P., *et al.* 1995, A&A 299, L168
28. Belokurov V., Evans N.W., Le Du Y. 2003, MNRAS, 341, 1373
29. Belokurov V., Evans N.W., Le Du Y. 2004, MNRAS, 352, 233
30. Bennett D. P., 2005, ApJ, 633, 906
31. Binney J., Gerhard 0., & Spergel D., 1997, MNRAS, 288, 365
32. Bissantz N., Englmaier P., Binney J., & Gerhard 0.E., 1997, MNRAS, 289, 651
33. Bond I.A., Abe F., Dodd R.J., et al., 2001, MNRAS, 327, 868
34. Brand J., Blitz L., 1993, A&A, 275, 67
35. Calchi Novati S., 2009, GRG, this volume, arXiv:0912.2667
36. Calchi Novati S., De Luca F., Jetzer Ph. and Scarpetta G., 2006, A&A, 459, 407
37. Calchi Novati S., De Luca F., Jetzer Ph. *et al.*, 2008, A&A, 480, 723
38. Calchi Novati S., Mancini L., Scarpetta G. and Wyrzykowski L., 2009, MNRAS 400, 1625
39. Dehnen W., and Binney J.J., 1998, MNRAS, 298, 387
40. Derue F., Afonso C., Alard C. *et al.* (EROS Coll.), 1999, A&A, 351, 87
41. Derue F., Afonso C., Alard C. *et al.* (EROS Coll.), 2001, A&A, 373, 126
42. De Rújula, A., Jetzer, Ph., and Massó, E. 1991, MNRAS, 250, 348
43. De Rújula, A., Jetzer, Ph., and Massó, E. 1992, A&A, 254, 99
44. Di Stefano R. and Esin A. A., 1995, ApJ, 448, L1
45. Dominik M., 2009, GRG, this volume.
46. Dong S., Udalski A., Gould A., et al., 2007, A&A, 664, 862
47. Dwek E., Arendt R.G., Hauser M.G. *et al.*, 1995, ApJ, 445, 716
48. Einstein A., Dec. 4, 1936, Science, New Series, Vol. 84, No. 2188., p. 506-507
49. Englmaier P., and Gerhard O., 1999, MNRAS 304, 512
50. Evans N.W. & Belokurov V., 2002, ApJ, 567, L119
51. Evans N.W. & Belokurov V., 2006, MNRAS, 374-1, 365
52. Feldman G.J. & Cousins R.D., 1998, Phys.Rev. D, 57, 3873
53. Freudenreich H.T., 1998, ApJ, 492, 495

54. Glicenstein J-F., 2003, ApJ, 584, 278
55. Gould, A. 1992, ApJ , 392, 442
56. Gould, A. 1995, ApJ, 446, L71
57. Gould A., Bahcall J.N., Flynn C., 1997, ApJ, 482, 913
58. Grenacher L., Jetzer P., Strässle M., and De Paolis F., 1999, A&A, 351, 775
59. Griest K. 1991, ApJ, 366, 412
60. Griest K., Thomas C. 2005, MNRAS, 359, 464
61. Gyuk G., Dalal N., Griest K., 2000, ApJ, 535, 90
62. Hamadache C., Le Guillou L., Tisserand P. et al., 2006, A&A, 454, 185
63. Hammersley P.L., Garzón F., Mahoney T., and Calbet X., 1995, MNRAS 273, 206
64. Han C., Gould A., 1995, ApJ, 449, 521
65. Han C., 1997, ApJ, 490,51
66. Hardy S.J. & Walker M.A., 1995, MNRAS, 276, L79
67. Hart J. et al., 1996, PASP, 108, 220
68. Jetzer, P., Mancini, L., and Scarpetta, G. 2002, A&A, 393, 129
69. Kerins, E., Robin, A. C., Marshall, D. J., 2009, MNRAS, 396(2), 1202
70. Le Guillou L. (EROS Coll.), 2002, Bull. of the AAS, 34, 717
71. Liebes S., 1964, Phys. Rev. 133, 835
72. LSST Science Book: arXiv:0912.0201
73. Lasserre T., Afonso C., Albert J.N. *et al.* (EROS Coll.) 2000, A&A 355, L39
74. Mancini L., Calchi Novati S., Jetzer P., Scarpetta G., 2004, A&A, 427, 61
75. Mao S., Stefano R.D., 1995, ApJ, 440, 22
76. Marshall, S. L. 1994, in Proceedings of IAU Symp. No. 161: Astronomy From Wide
    Field Imaging, p. 67. ed. H. T. MacGillivray *et al.* (Dordrecht: Kluwer Academic Publ.)
77. MicroFUN web-page: `http://www.astronomy.ohio-state.edu/~microfun/`
78. MINDSTEp web-page: `http://www.mindstep-science.org/`
79. Möllerach S., Roulet E., 2002, Gravitational lensing and microlensing, World Scientific
80. Muraki Y., Sumi T., Abe F., 1999, Prog. Theor. Phys. Suppl., 133, 233
81. Paczyński B., 1986, ApJ, 304, 1
82. Paczyński B., Stanek K. Z., 1998, ApJ, 494, L219
83. Palanque-Delabrouille N., Afonso C, Albert J.-N., et al, 1998, A&A 332, 1
84. Picaud S., Robin A.C., 2004, A&A, 428, 891
85. PLANET web-page: `http://planet.iap.fr/`
86. Popowski, P., Griest, K., Thomas, C. L., *et al.*, 2005, ApJ, 631, 879
87. Rahal Y. R., 2009, A&A 500, 1027
88. Rahvar S., Moniez M., Ansari R. and Perdereau O., 2003, A&A 412, 105
89. Reid, I. N., Sahu, K. C., & Hawley, S. L. 2001, ApJ, 559, 942
90. Renault, C. *et al.* (EROS Coll.) 1997, A&A, 324, L69
91. Renault, C. *et al.* (EROS Coll.) 1998, A&A, 329, 522
92. Renn J., Sauer T., Stachel J., 1997, Science, 275, no. 5297, 184
93. Rest A., Stubbs C., Becker A.C. et al., 2005, ApJ, 634, 1103
94. Rhie S.H., Becker A.C., Bennett D.P., et al., 1999, ApJ, 522, 1037
95. Sahu, K.C., 1994, Nature, 370, 275
96. Sahu, K.C., 1994, PASP, 106, 942
97. Sahu K. C. and Sahu M.S., 1998, ApJ 508 L147
98. Sako T., Sekiguchi T., Sasaki M. et al., Experimental Astronomy 2008, 22, 51
99. Schechter P.L., Mateo M. and Saha A. 1993, PASP, 105, 1342
100. Schneider P., Kochanek C., Wambsganss J., "Gravitational Lensing: Strong, Weak and
     Micro.", 2006, Springer
101. Stanek K.Z., Udalski A., Szymański M., 1997, ApJ, 477, 163
102. Stubbs, C. W., *et al.* 1993, Proc. SPIE, 1900, 192
103. Sumi T., Kan-ya Y., MNRAS, 2002, 337, 1017
104. Sumi T. *et al.*, 2003, ApJ, 591, 204
105. Sumi T., Wozniak P. R., Udalski A. *et al.* (OGLE coll.), 2006, ApJ, 636, 240
106. Tisserand P. *et al.*, 2007, A&A, 469, 387
107. Udalski A., 2003, Act. Astr., 53, 291
108. Udalski A., Kubiak M. and Szymański M., 1997, Act. Astr 47, 319
109. Udalski A., Kubiak M., Szymański M. *et al.* (OGLE Coll.), 1998, Act. Astr. 48, 431.
110. Udalski A., Szymański M., Kaluzny J. *et al.* (OGLE Coll.), 1993, Act. Astr., 43, 69

111. Udalski A., Szymański M., Kaluzny J. *et al.* (OGLE Coll.), 1993, Act. Astr., 43, 289
112. Udalski A., Szymański M., Stanek K.Z. *et al.* (OGLE Coll.), 1994, Act. Astr. 44, 165.
113. VISTA web-page:http://www.vista.ac.uk/
114. VVV proposal available on web-page: http://vvvsurvey.org/
115. Wozniak P. et al., 2001, Act. Astr., 51, 175
116. Wozniak P., Paczyński B., 1997, ApJ, 487, 55
117. Wyrzykowski L., Kozlowski S., Skowron J., et al., 2009, MNRAS 397, 1228
118. Xu J., Crotts A. P. S., and Kunkel W. E., 1995, ApJ, 451, 806
119. Yanagisawa, T., Muraki Y., Matsubara Y., et al., 2000, Exp. Astron., 10, 519
120. Yoo et al., 2004, ApJ, 603, 139-151
121. Zhao H-S. and de Zeeuw P.T. 1998, MNRAS 297, 449
122. Zoccali M., Cassisi S., Frogel J.A. *et al.* 2000, ApJ 530, 418.